Journal of Inorganic Biochemistry 200 (2019) 110803

Contents lists available at ScienceDirect

Journal of Inorganic Biochemistry

journal homepage: www.elsevier.com/locate/jinorgbio

Antiproliferative evaluation and supramolecular association in Mn(II) and Zn(II) bipyridine complexes: Combined experimental and theoretical studies

Manjit K. Bhattacharyya[a,*], Anshuman Gogoi[a], Sanjib Chetry[a], Debajit Dutta[a], Akalesh K. Verma[b], Bipul Sarma[c], Antonio Franconetti[d], Antonio Frontera[d,*]

[a] Department of Chemistry, Cotton University, Guwahati 781001, Assam, India
[b] Department of Zoology, Cell & Biochemical Technology Laboratory, Cotton University, Guwahati 781001, Assam, India
[c] Department of Chemical Sciences, Tezpur University, Tezpur 784028, Assam, India
[d] Departament de Química, Universitat de les Illes Balears, Crta de valldemossa km 7.7, 07122 Palma de Mallorca, (Baleares), Spain

ARTICLE INFO

Keywords:
Cooperativity
π–π stacking
T-cell lymphoma
Cytotoxicity
Apoptosis
Docking

ABSTRACT

Two new coordination complexes viz. $[Mn_2(\mu\text{-}O,O'\text{-}4\text{-}Mebz)_2(bpy)_2(\mu^2\text{-}H_2O)(4\text{-}Mebz)_2]$ (**1**) and $[Zn(bpy)(pdc)(H_2O)]\cdot 3.5H_2O$ (**2**) (where bpy = 2,2′-bipyridine, 4-Mebz = 4-methyl benzoate and pdc = 2,6-pyridine dicarboxylate) were synthesized and structurally characterized by single crystal X-ray diffraction, FT-IR, electronic spectroscopy, Thermogravimetric Analysis (TGA) and Powder X-ray diffraction (PXRD) techniques. Complex **1** consists of a dinuclear Mn(II) unit bridged by a solvent water molecule while **2** is a mononuclear complex. The supramolecular assemblies found in the solid state of both complexes have been described. In **2**, several π-stacking interactions modes have been further studied using Density Functional Theory (DFT) calculations. Furthermore, the activity of the complexes against a few pathogenic bacteria has been studied and confirmed. Finally, the antiproliferative activities of both complexes have been studied in *T-cell lymphoma* cell line by 3-(4,5-dimethylthiazol-2-yl)-2,5-diphenyltetrazolium bromide (MTT) assay, apoptosis assay and molecular docking simulation. Both the complexes exhibit gratifying cytotoxicity through apoptotic cell death with negligible cytotoxicity (~5–10%) in normal cells. It is worth mentioning that Mn(II) and Zn(II) complexes exhibit interaction modes with highly expressed cancer target proteins under study with *higher* binding *affinity* and the results are comparable with reference inhibitors.

1. Introduction

Mononuclear and dinuclear transition metal complexes and ligands have been extensively investigated because of their potential applications in bioinorganic chemistry, magnetochemistry, materials chemistry and catalysis [1–2]. Multidentate N- and O-donor ligands have been widely used to form such multinuclear species. In particular, dinuclear structures containing two Mn(II) ions have been proposed as reliable models of pseudocatalase and ribonucleotide reductase (RR) as well as useful precursors to high nuclearity clusters [3]. Among them, particular attention has been paid to water- and/or carboxylate-bridged complexes where metal-metal distances span from 3.3 to 4.3 Å [4] similar to the value of 3.6 Å found in the catalase [5].

The applications of metal complexes derived from pyridine dicarboxylic acid (pdc) ligand are diverse, including material chemistry [6–7], medicine [8–9] and biology [10–11]. Due to the multiple coordination modes of the pyridine dicarboxylate anions, metal pyridine dicarboxylate complexes show large structural varieties [12–15]. Further interest on structure determinations of such complexes arises from the occurrence of their different hydrates [16–17]. Several metal-containing compounds have been utilized throughout history to treat a wide variety of human ailments. Almost all living organism make extensive use of metal ions, such as zinc and copper, which play major roles in the normal physiological processes [18]. Copper, iron, and manganese and others transition metals are involved in multiple biological processes, from electron transfer to catalysis to structural roles, and are frequently associated with active sites of many proteins and enzymes [18]. Since the discovery of cisplatin and associated analogues as a potent anticancer drug, the coordination chemistry of metal-based drugs have *generated* interest among researchers due to its various applications in cancer management [19–21]. It is well known that *cisplatin* is a metal-based chemotherapy medication used to treat a number of cancers, at the same time; it possesses severe side effects in the host including renal damage and hematotoxicity and acquired drug

* Corresponding authors.
E-mail addresses: manjit.bhattacharyya@cottonuniversity.ac.in (M.K. Bhattacharyya), toni.frontera@uib.es (A. Frontera).

https://doi.org/10.1016/j.jinorgbio.2019.110803
Received 9 April 2019; Received in revised form 7 August 2019; Accepted 18 August 2019
Available online 20 August 2019
0162-0134/

resistance [22]. Severe side effects and drug resistance features of available anticancer drugs *come into view* as obstacles to a successful chemotherapy. Therefore, it is of continuous interest the research and development of potent metal-based anticancer drugs, which is an essential area in the field of drug discovery [23]. Most of the clinically approved anticancer drugs are molecules which induce DNA damage or block DNA synthesis, or inhibit key enzymes and proteins involved in cell division and growth [24]. So nowadays, considerable effort has been put forward for the development of novel anticancer agents based on human compatible metal complexes with lesser toxicity, more efficacious and target-specific.

Herein, we report two coordination complexes of Mn(II) and Zn(II) viz. $[Mn_2(\mu\text{-}O,O'\text{-}4\text{-}Mebz)_2(bpy)_2(\mu^2\text{-}H_2O)(4\text{-}Mebz)_2]$(**1**) and $[Zn(bpy)(pdc)(H_2O)]\cdot 3.5H_2O$ (**2**) (where bpy = 2,2′-bipyridine, 4-Mebz = 4-methylbenzoate and pdc = 2,6-pyridinedicarboxylate). A detail structural analysis reveals cooperative supramolecular interactions in the solid state of **1** and **2**. In the crystal structure of **1**, C—H···C contacts along with C—H···O and π–π stacking interactions leads to the self-assembly of **2** into a layered supramolecular architecture. In the solid-state structure of **2**, the monomeric units are arranged into a 2D architecture involving cooperative interplay of weak interactions viz. π–π stacking and C—H···O hydrogen bonding interactions. More importantly, the manuscript aims to perform a small pharmacological screening regarding two of the most interesting pharmacological groups nowadays: antimicrobials and anticancer. In particular, the anticancer activity of both the compounds has been evaluated against T-Cell lymphoma malignant cancer cell line by MTT [3-(4,5-dimethylthiazol-2-yl)-2,5-diphenyltetrazolium bromide] and apoptosis assays and molecular docking simulations. The antibacterial activity has been evaluated towards Rhizobium Leguminosarum, Staphylococcus aureus and *E. coli*.

2. Experimental

2.1. Material and methods

All reagents viz. Manganese(II) chloride tetrahydrate, zinc(II) chloride, 2,2′-bipyridine, 4-methylbenzoic acid and 2,6-pyridine dicarboxylic acid used in this work were obtained from Sigma Aldrich and Merk (India) Ltd. and used as received. Deionised water was used as a reaction medium throughout the experiments. Elemental analyses (C, H and N) were carried out using a Perkin Elmer 2400 Series II CHN Analyzer. KBr phase FT-IR spectra were recorded in a Shimadzu FTIR-8400 spectrophotometer in the mid-IR region (4000 to 400 cm^{-1}). The electronic spectra were recorded using a Shimadzu UV-2600 spectrophotometer. For UV–vis-NIR spectrum, $BaSO_4$ powder was used as reference (100% reflectance). Thermogravimetric studies were carried out under a flow of N_2 gas (25–700 °C) using a METLER TOLEDO Thermal Analyzer at a heating rate of 10 °C min^{-1}. The Powder X-ray diffraction (PXRD) data was recorded using a XPERT-PRO X-ray powder diffractometer with Cu-Kα radiation. The data was collected over the range of 2–90° 2θ at a continuous scanning speed. Room temperature magnetic susceptibility was measured at 300 K on a Sherwood Mark 1 Magnetic Susceptibility balance by Evans Method.

2.2. X-ray crystallography

Crystals of desired quality for single crystal X-ray diffraction studies for complexes **1** and **2** were obtained from the mother liquor upon slow evaporation. Intensity data collection for chosen crystals was done on a Bruker SMART CCD Diffractometer. Using a full set of unique data corrected for absorption using SADABS, the crystal structures were solved by direct method and refined by full-matrix least squares techniques with SHELXL-97 [25] via WinGX [26]. All non-hydrogen atoms were refined anisotropically. The hydrogen atoms were found via difference Fourier synthesis and they were refined isotropically. The hydrogen atoms, except those attached to oxygen atoms of water molecules in **2** were placed at their calculated positions and refined in the isotropic approximation; those attached to hetero-atoms (O) were located in the difference Fourier maps, and refined with isotropic displacement coefficients. The hydrogen atom of lattice water (O6) could not be located in the structure **2**. The structural diagrams were drawn with Diamond 3.2 [27]. Crystallographic results for complexes **1** and **2** are summarized in Table S1.

2.3. Computational methods

The calculations of the noncovalent interactions and molecular electrostatic potential (MEP) surfaces were carried out using the Gaussian-09 [28] and the M06-2X/def2-TZVP level of theory. The Grimme's dispersion correction has been used in the calculations [29]. To evaluate the interactions in the solid state, the crystallographic coordinates were used and only the position of the H-atoms has been optimized. This procedure and level of theory has been successfully used to evaluate similar interactions [30]. The interaction energies were computed by calculating the difference between the energies of the isolated monomers and their assembly. The NCI (Non-Covalent Interaction Index) plot is a visualization index that efficiently allows the identification and visualization of non-covalent interactions [31]. It is based on the electron density and its derivatives and the isosurfaces correspond to both favorable and unfavorable interactions. They are easily differentiated by the sign of the second density Hessian eigenvalue and defined by the isosurface color. The NCI analysis is a very convenient tool to rationalize host–guest complementarity and to know which interactions stabilize a complex. The color scheme is a red-yellow-green-blue scale with red for ρ_{cut}^{+} (repulsive) and blue for ρ_{cut}^{-} (attractive). Yellow and green surfaces correspond to weak repulsive and weak attractive interactions, respectively [32].

2.4. Synthesis of complexes

2.4.1. Synthesis of $[Mn_2(\mu\text{-}O,O'\text{-}4\text{-}Mebenz)_2(bpy)_2(\mu^2\text{-}H_2O)(4\text{-}Mebenz)_2]$ (**1**)

A mixture of $MnCl_2{\cdot}4H_2O$ (0.197 g, 1 mmol), bpy (0.156 g, 1 mmol) and sodium salt of 4-Mebz (0.204 g, 1 mmol) in 20 mL water was mechanically stirred for 2 h at room temperature. The light yellow product so formed was filtered, washed with water followed by diethylether and dried in a vacuum desiccator over fused $CaCl_2$. Yellow block crystals suitable for single crystal X-ray diffraction were obtained from the mother liquor after few months. Yield: 85% (0.34 g). Anal. Calcd. for $C_{52}H_{46}Mn_2N_4O_9$: C, 63.68; H, 4.73; N, 5.71; Found: C, 63.73; H, 4.64; N, 5.73, %.FT-IR spectral data (KBr disc, cm^{-1}): 3446(br), 3057(m), 2917(m), 2858(w), 2521(w,sh), 2398(w), 2292(b), 2036(b), 1925(sh), 1602(s), 1557(s), 1476(s), 1446(sh), 1389(s), 1314(s), 1223(s), 1176(s), 1095(s), 1042(sh), 1014(s), 961(sh), 845(s), 764(s), 705(m),646(sh), 610(s), 551(m) [s, strong; m, medium; w, weak; br, broad; sh, shoulder].

2.4.2. Synthesis of $[Zn(bpy)(pdc)(H_2O)]\cdot 3.5H_2O$(**2**)

A mixture of $ZnCl_2$ (0.136 g, 1 mmol), bpy (0.156 g, 1 mmol) and disodium salt of pdc (0.211 g, 1 mmol) in 20 mL water was mechanically stirred for 2 h at room temperature. The white product so formed was filtered, washed with water followed by diethylether and dried in a vacuum desiccator over fused $CaCl_2$. White block crystals suitable for single crystal X-ray diffraction were obtained from the mother liquor after several days. Yield: 85% (0.34 g). Anal. Calcd. for $C_{34}H_{40}ZnN_6O_{17}$: C, 46.93; H, 4.63; N, 9.66; Found: C, 46.92; H, 4.62; N, 9.61, %.FT-IR spectral data (KBr disc, cm^{-1}): 3418(br), 3095(m), 2917(m), 2858(w), 2521(w,sh), 2398(w), 2292(b), 2036(b), 1925(sh), 1602(s), 1557(s), 1476(s), 1446(sh), 1395(s), 1314(s), 1223(s), 1176(s), 1095(s), 1042(sh), 1020(s), 961(sh), 845(s), 764(s), 705(m),646(sh), 610(s), 551(m) [s, strong; m, medium; w, weak; br, broad; sh, shoulder].

2.5. MTT cell viability assay and IC_{50} measurement

The MTT assay is a colorimetric assay and is most commonly used for measuring cell viability and cell proliferations [33]. It is based on the ability of cellular oxidoreductase enzymes in presence of nicotinamide adenine dinucleotide phosphate (NADPH) to reduce the tetrazolium, *MTT* salt into insoluble formazan crystal, which ultimately produces purple color with DMSO. In the present study cell viability was measured by the same assay in T cell lymphoma and peripheral blood mononuclear cells (PBMC) (normal cells) according to the instructions in the Cell Proliferation Kit (MTT, manual from Boehringer Mannheim, Cat. No. 1465 007) [34]. In brief, after incubation with different doses (0, 100, 200, 300, 400 and 500 μg/mL) of complex, **1** and **2** for 24 h, 10 μL of the MTT labeling reagent (5 mg/mL in phosphate-buffered saline) was added into each well except the empty wells. The microtiter plate was then incubated for four hours under 5% CO_2 and 95% air at 37 °C. Following that, 100 μL of the DMSO was poured into each well and gently shaken. The plate was checked for complete solubilization of crystal followed by measurement of absorbance of all the samples at the wavelength of 550 nm. The percentage of cell viability was calculated with the following formula:

A dose-response curve (sample concentration in X-axis versus % cell viability in Y-axis) was plotted and the sample concentration that inhibits 50% of the cell viability (IC_{50}) was determined using the linear equation ($y = mx + n$) considering $y = 50$ and the obtained value at x point becomes IC_{50} value [35].

2.6. Apoptosis study using fluorescence microscope

Complexes **1** and **2** mediated apoptotic cell death was assessed by using acridine orange/ethidium bromide (AO/EB) double staining method [36]. Acridine orange is taken up by both viable and apoptotic cells and emits green fluorescence when exposed to UV light. Ethidium bromide is taken up only by apoptotic cells and emits red fluorescence. In present study, control and treated cancer cells were collected after 24 h treatment, washed with PBS and to the cell suspension; 20 μL of AO/EB dye mixture (100 μg/mL of each dye in distilled water) was added, mixed gently and incubated for 5 min in dark. The cells were thoroughly examined under fluorescence microscope and photographed. About 1000 cells were analyzed, and the percentage of apoptotic nuclei was determined for three independent determinations based on differential coloring pattern of nuclei. Viable cells were identified by bright uniform green nuclei with organized structures; apoptotic cells contain condensed or fragmented chromatin with red or orange nuclei [37].

2.7. Molecular docking study

In the present molecular docking study, Molegro Virtual Docker (MVD) software (www.molegro.com) along with Graphical User Interface (GUI), MVD tools was utilized to generate grid, calculate dock score and evaluate conformers [38]. The three dimensional (3D) coordinates of various cancer target proteins were selected and obtained through the internet at the Research collaborator for Structural Bioinformatics (RCSB) protein data bank (PDB). The PDB id of 4XV2 (melanoma, colorectal, thyroid and Non-small cell lung cancer), 5LWE (ovarian cancer, prostate cancer, pancreatic cancer, Large B cell lymphoma, Melanoma), 4FLH (Colon, brain, gastric, breast and lung cancer), 1XKK (Non-small cell lung cancer, (bladder cancer, breast cancer and glioblastoma) were selected based on the potential roles in multiple cancer types [39–42]. The molecular arrangement and geometry of the complexes were fully optimized using the semi empirical quantum chemistry method (PM3). All of the water and cofactors compounds were deleted from the protein structures, and the protein and ligands structures were further prepared using the parameter settings in the same software package [43]. The scoring function used by MolDock is derived from the Piecewise Linear Potential (PLP) scoring functions. The active binding site region was defined as a spherical region which encompasses all protein within 15.0 Å of bound crystallographic ligand atom with selected coordinates of X, Y and Z axes, respectively. Default settings were used for all the calculations. Docking was performed using a grid resolution of 0.30 Å and for each of the 10 independent runs; a maximum number of 1500 iterations were executed on a single population of 50 individuals. The active binding site was considered as a rigid molecule, whereas the ligands were treated as being flexible, i.e. all non-ring torsions were allowed [38]. Protein-ligand interaction was further analyzed and visualized by Chimera software (https://www.cgl.ucsf.edu/chimera/). In modern computational and medicinal chemistry, pharmacophore features are used to identify the essential components of one or multiple molecules with the similar biological activity [44]. Pharmacophore features are very useful signature of chemical compounds which can be used to search for more molecules which share the same features arranged in the same 3D orientation. In the present study, pharmacophore models of both the complexes were generated using Ligandscout software which demonstrated Structural Activity Relationship (SAR) [45]. After performing molecular docking simulation, the obtained best docking orientation (pose) were loaded into Ligandscout software and key pharmacophore features were identified including H-bond donor, H-bond acceptor, Hydrophobic, aromatic, positively and negatively ionizable groups.

2.8. Statistical analysis

Experimental results are expressed as mean ± S.D. All measurements were replicated three times. The data were analyzed by an analysis of variance (ANOVA) ($P \leq 0.05$). The IC_{50} values were calculated from linear regression analysis.

2.9. Antimicrobial study

The antimicrobial activity of compounds **1**, **2**, ligand bpy and the metal salts ($MnCl_2{\cdot}4H_2O$ and $ZnCl_2$) were studied by the disc diffusion method against the pathogenic organisms [*Staphylococcus aureus* (MTCC3160), *Escherichia coli* (MTCC448), Rhizobium leguminosarum (MTCC99) and Rhizoctonia solani (MTCC4633)]. All the experiments were performed in Petri plates and were repeated twice. Nutrient agar (Himedia) was used as a media for bacterial growth while potato dextrose agar (PDA) was used as media for fungi (Hi-media). All the sterilized materials were kept under the Laminar Air Flow (Sensocon/S2000-25MM). The test cultures were spread using L spreader on the top of the solidified media and kept for 10 min and the complexes, ligands and metal salts of concentrations 125 μg mL^{-1}, 150 μg mL^{-1}, 250 μg mL^{-1}, 300 μg mL^{-1},350 μg mL^{-1}, 400 μg mL^{-1}, and 450 μg mL^{-1} were added to each disc. The cultures were incubated at 37 °C for 24 h (bacteria) and at 28 °C for three days (fungi) in an incubator (Scigenics-Orbitek BOD-350 L). DMSO was used as a negative control in the experiments. Ofloxacin (antibacterial) (5 μg per disc) and Ketoconazole (antifungal) (10 mg per disc) was used as positive control [46]. The diameters of the inhibition zones were measured following the incubation period with slipping calipers recorded in millimeter. The antimicrobial results of the compounds were compared with the standard and % activity index for the compounds was calculated by using the formula as given below:

$$\%\text{Activity index} = \frac{\textit{Zone of inhibition by the test compound (mm)}}{\textit{Zone of inhibition by standard (mm)}} \times 100$$

3. Results and discussion

3.1. Synthesis and general aspects

The complex $[Mn_2(\mu\text{-O,O}'\text{-4-Mebenz})_2(bpy)_2(\mu^2\text{-}H_2O)(4\text{-Mebenz})_2]$ (**1**) has been isolated in good yield by reacting one equivalent of

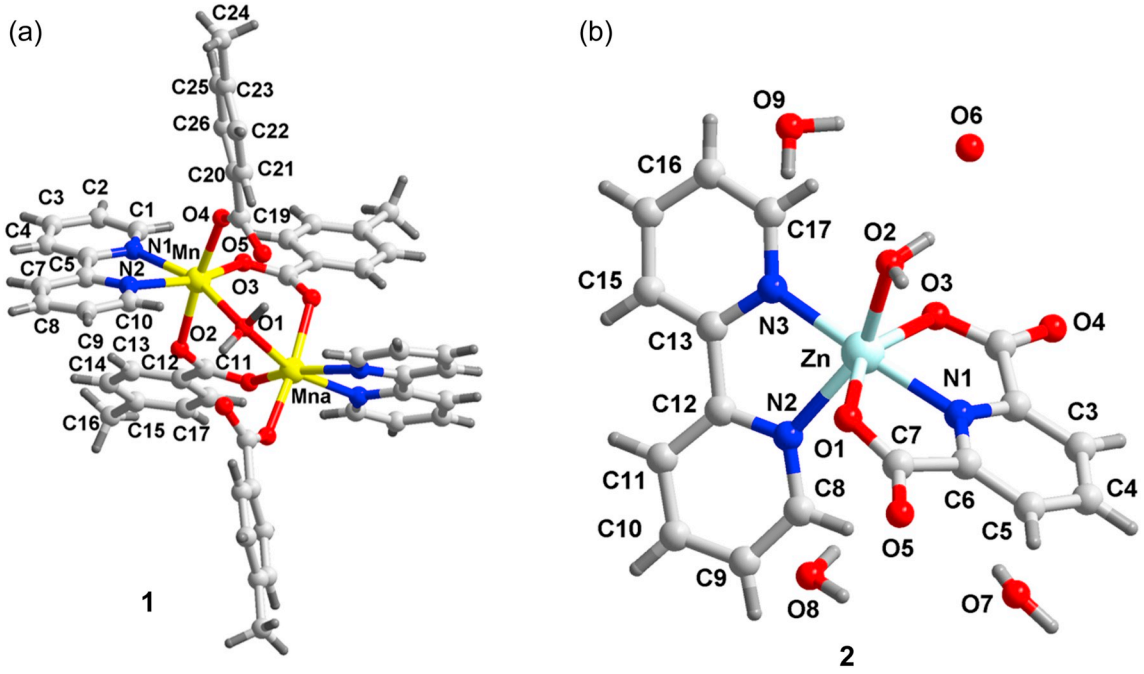

Fig. 1. Molecular structures of **1** (a) and **2** (b) with atom labeling scheme.

$MnCl_2{\cdot}4H_2O$ with one each equivalent of bpy and 4-Mebz in aqueous medium. The complex $[Zn(bpy)(pdc)(H_2O)]{\cdot}3.5H_2O$ (**2**) is obtained by reacting one equivalent of $ZnCl_2$ with one equivalent each of bpy and pdc in aqueous medium. Complexes **1** and **2** are soluble in water and also in common organic solvents viz. methanol, DMSO etc. The complex **1** shows room temperature μ_{eff} value of 5.69 BM and confirms the presence of five unpaired electrons in the Mn(II) centers. Both complexes have been characterized using different spectroscopic methods (IR, UV, PXRD) and thermogravimetric analysis (see supplementary information file, Figs. S1 to S6).

3.2. X-ray structures of complexes *1* and *2*

The structure of **1** is shown in Fig. 1a together with the atomic numbering scheme. Selected bond lengths and angles are summarized in Table S2. The crystal structure of **1** consists of a discrete dinuclear unit of formula $[Mn_2(bpy)_2(4\text{-Mebz})_2(H_2O)]$ where each of the manganese centers has octahedral geometry involving two bridging 4-Methylbenzoate groups (Fig. 1a), two coordinated bpy molecules and a monodentate 4-Methylbenzoate apart from a bridging solvent water molecule. The Mn···Mn^a distance in this complex is 3.5501(8) Å. The monodentate benzoate groups are intramolecularly hydrogen-bonded to the bridging water through O(1)—H···O(3) [2.569(3) Å, 142.2(3)°] interactions. The Mn—O(1) and Mn^a—O(1) bond lengths in this complex are 2.252(3)Å while the corresponding Mn—O(1)—Mn^a bond angle is 104.06(1)°. Each of the two manganese centers, present distorted octahedral environment, being coordinated to the bpy ligand through the nitrogen atoms N(1), N(2) and the phenoxo oxygen atoms O(4) and O (4a) respectively with usual bond distances (Table S2). The carboxylate oxygen atoms O(4) and O(4a) of the terminally coordinated monodentate benzoate ions, the oxygen atom O(1) of the water molecule and the bridging phenoxo atoms O(2) and O(3) complete the hexa coordination of the Mn(II) centers respectively. Various weak intermolecular interactions such as π–π stacking and C—H···O hydrogen bonding interactions govern the crystal solid state structure of **1** and are detailed in the ESI (Fig. S7).

The crystal structure of **2** comprises a Zn(II) metal center, one pdc^{2-} ligand, one bpy molecule and a coordinated water molecule. As shown in Fig. 1b, the Zn(II) ion is coordinated to two monodentate carboxylate groups from one pdc^{2-} ligand, one nitrogen atom (N1) from the pyridine ring of one pdc^{2-} ligand and two nitrogen atoms (N2) and (N3) of bipyridine. One mononuclear complex unit (Z = 1) with three lattice water molecules along with a water molecule of half occupancy constitutes the asymmetric unit of **2**. The variation of the bond angles [73.33(1)–165.02(1)] indicates a significant distortion from ideal octahedral geometry, the Zn—O and Zn—N bond lengths are in the typical ranges 2.10–2.25 and 2.04–2.14 respectively [47–48].

A careful look at the packing of the molecules in the crystal lattice of **2** reveals the formation of extensive O—H···O and C—H···O hydrogen bonding interactions along with π–π stacking interactions in the direction of crystallographic *ac* plane leading to the formation of a supramolecular layered structure (Fig. 2). The coordinated water molecule (O2) participates in intermolecular O—H···O hydrogen bonds with the uncoordinated oxygen atom (O4) of the pdc ligand. The O—H···O bond distance is 1.891 Å. The coordinated water molecule (O2) also participates in intermolecular C—H···O hydrogen bonding interaction with carbon atom (C3) of the bpy ligand having C—H···O bond distance of 2.863 Å. In complex **2**, two types of π–π stacking interactions between the bpy ligands are established [denoted as $(\pi\text{–}\pi)_1$ and $(\pi\text{–}\pi)_2$] that generate the formation of infinite 1D columns in the solid state. Remarkably, these columns are connected by another type of π–π stacking interaction $(\pi\text{–}\pi)_3$ between the pdc ligands. The ring centroid-centroid distance is 3.566 Å. The energetic features of these interactions are studied below. Further description of the solid state structure of **2** is included in the ESI (see Fig. S8).

3.3. Theoretical study

The theoretical study is devoted to the analysis of the three different types of intermolecular π–π stacking interactions that are crucial to understand the crystal packing of compound **2** as described in Fig. 2. First of all, we have computed the molecular electrostatic potential (MEP) plotted onto the van der Waals surface (isosurface 0.001 a.u.) in order to investigate the electron rich and electron poor regions of compound **2** (see Fig. 3). The most positive region is located at the coordinated water molecule (+56 kcal/mol). This is due to the coordination of the water to the Zn(II) metal center that significantly increases the acidity of the H atoms. The most negative region is located

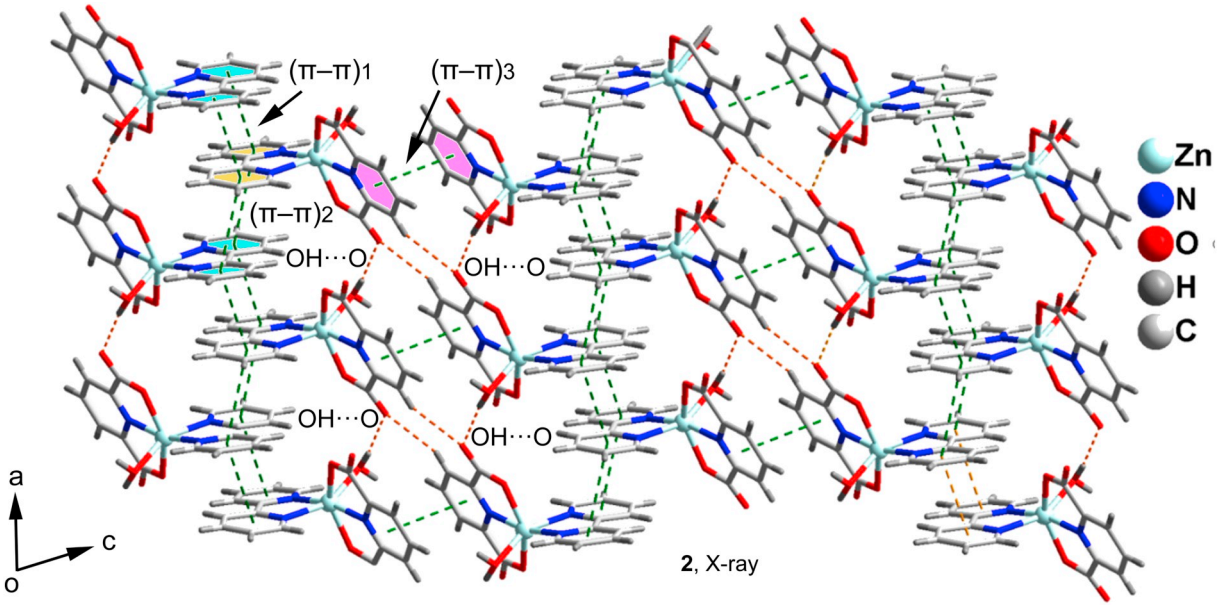

Fig. 2. Perspective view of a 2D supramolecular architecture generated by O—H···O, C—H···O and π–π stacking interactions. Lattice water molecules are omitted for clarity. (Orange dotted lines represent O—H···O and C—H···O hydrogen bonding interactions and green dotted lines represents π–π stacking interactions).

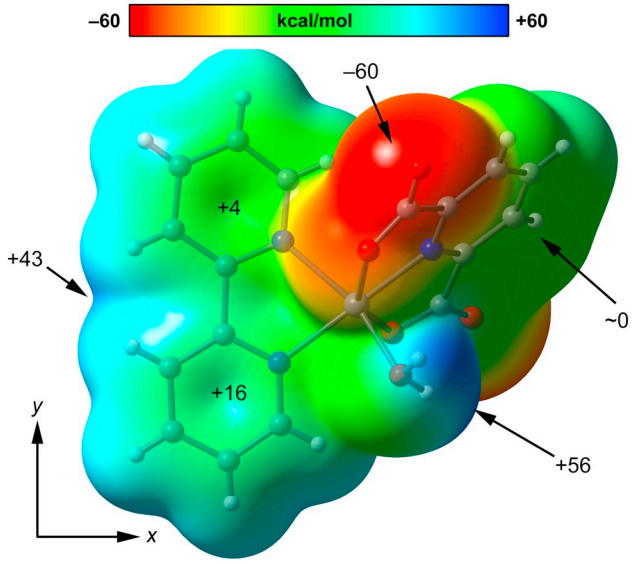

Fig. 3. MEP surface of compound **2** at the M06-2x/def2-TZVP level of theory using the 0.001 a.u. isosurface. The values at selected points of the surface are indicated in kcal/mol.

at the O-atoms of the dianionic ligand, as expected. Therefore, the most favored interaction from an electrostatic point of view is an H-bond between the Zn—OH_2 and the carboxylate group. This interaction is indeed observed in the solid state of compound **2** (see red dashed lines in Fig. 2). Moreover, the inspection of the MEP surface also reveals that the MEP at the aromatic H-atoms of the bipyridine ligand is positive (+46 kcal/mol), thus adequate for establishing H-bonding interactions with electron rich regions or atoms. The MEP over the π-system of the pdc ligand is negligible and over the bipyridine π-system is positive (+4 and +16 kcal/mol, see Fig. 3). The charge distribution over the bipyridine ring indicate that anti-parallel (in both *x* and *y* directions, see Fig. 3) π-stacking interactions is preferred to minimize electrostatic repulsions and maximize dipole···dipole interactions.

We have studied the energetic features of the three π-stacking interactions described for compound **2** and the results are summarized in Fig. 4a–c. The assembly denoted as $(\pi–\pi)_1$ is the most favorable with a binding energy of $\Delta E_1 = -27.0$ kcal/mol. This large binding energy is due to the large overlap of the two π-systems along with some additional C—H···O interactions as described below. The $(\pi–\pi)_2$ assembly also presents a large interaction energy $\Delta E_2 = -16.4$ kcal/mol, however it is less favored than $(\pi–\pi)_1$ likely due to longer π–π distance (3.884 Å) and a lesser contribution of the ancillary C—H···O interactions. Finally, the energy of the $(\pi–\pi)_3$ is more modest, due to the smaller π-system and absence of ancillary interactions. Nevertheless, the interaction energy ($\Delta E_3 = -7.5$ kcal/mol) is strong compared to conventional π-stacking interactions, which is due to the coordination of the aromatic ring to the metal center, that significantly increases the dipole···dipole contribution.

In order to further characterize the π–π assemblies we have used the NCI plot index. Non-covalent interactions are efficiently visualized and identified by using the NCI plot tool. It allows an easy assessment of host–guest complementarity and the extent to which weak interactions stabilize a complex. We have computed the NCI plots for the three π-stacking dimers, which are represented in Fig. 4 (using a zenithal orientation). For the $(\pi–\pi)_1$ dimer, a green isosurface can be observed between both π-systems that embraces the whole bpy ligand, thus suggesting a large overlap of the aromatic rings. Moreover, two small and blue isosurfaces are also present that characterize the intramolecular C—H···O bonds. This isosurface is located between the carboxylate group and the aromatic H atoms of the bipyridine ligand. The existence of this interaction agrees well with the MEP surface shown in Fig. 3 that reveals a large and positive MEP value at this region of the bpy ligand. The presence of these strong H-bonds explains the large interaction energy obtained for this dimer. The NCI plot of $(\pi–\pi)_2$ dimer also shows a large and green isosurface between the π-systems. Compared to $(\pi–\pi)_1$ dimer the shape of the surface indicates that the overlap of the π-system is smaller (fragmented isosurface), in line with the smaller binding energy. Moreover, the C—H···O interactions are characterized by green isosurfaces, thus indicating that they are weaker compared to $(\pi–\pi)_1$. Finally, the NCI plot of $(\pi–\pi)_3$ dimer shows a significant overlap of both π-systems and the absence of ancillary interactions, in agreement with the interaction energy.

3.4. Antimicrobial study of the complexes

The antimicrobial activity of the complexes **1**, **2** and the common

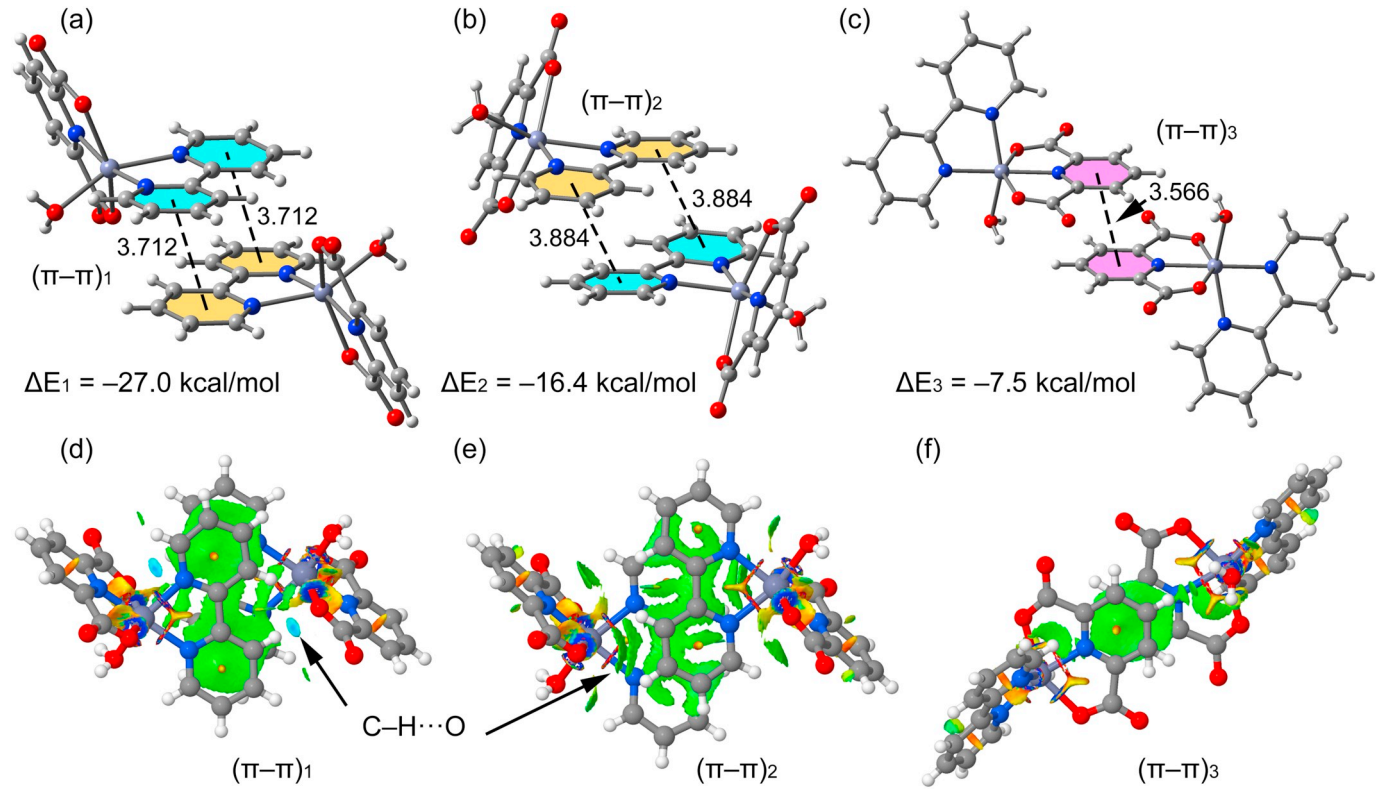

Fig. 4. (a–c) Interaction energies and geometric features of the three stacked dimers of **2**. Distances in Å measured between the ring centers (d–e) NCI plots of the (zenithal view) of the three π-stacked dimers of compound **2**. The gradient cut-off is s = 0.35 au, and the color scale is $-0.04 < \rho < 0.04$ au.

ligand bpy were tested against four pathogenic organisms viz. *Rhizobium Leguminosarum* (MTCC99), *E. coli* (MTCC448), *Staphylococcus aureus* (MTCC-3160) and *Rhizoctonia Solani* (MTCC4633) by disc diffusion method. The antimicrobial activity of the metal salts ($MnCl_2{\cdot}4H_2O$ and $ZnCl_2$) has also been investigated. It has been found that the metal salts do not exhibit antimicrobial activity, at the concentration range used to assay the activity of the complexes in this work [49]. Moreover, the ligands 4-Mebz [50] and pdc showed hardly any activity [51]. The zone of inhibition (Table 1) exhibited by the complexes and the bpy ligand at different concentrations are summarized in Fig. 5. The results are compared with the standard antibacterial (Ofloxacin) and % activity index was tabulated in Table 1. Among the three bacterial cultures, both the complexes and ligand showed antibacterial activity towards *Rhizobium Leguminosarum* (MTCC99), *Staphylococcus aureus* (MTCC-3160) and *E. coli* (MTCC448) under assay conditions. The minimum inhibitory concentration (MIC) values for the complexes and ligand are summarized in Table 2. The MIC values revealed that the complexes have relatively better antibacterial activity compared to the free ligand. According to Overtone's concept of cell permeability, the lipid membrane that surrounds the cell favors the passage of only lipid-soluble substances, so lipophilicity is an important factor controlling the antimicrobial activity. Upon chelation, the polarity of the metal ion is reduced due to the overlap of ligand orbitals and partial sharing of its positive charge with the donor groups thereby increasing the lipophilic nature of the central metal ion, which in turn favors its permeation into the lipid layer of the membrane [52]. Furthermore, chelation allows delocalization of π-electrons over the entire chelate ring and enhances the lipophilicity of the complexes. Both the complexes as well as the ligand were also screened against the fungi

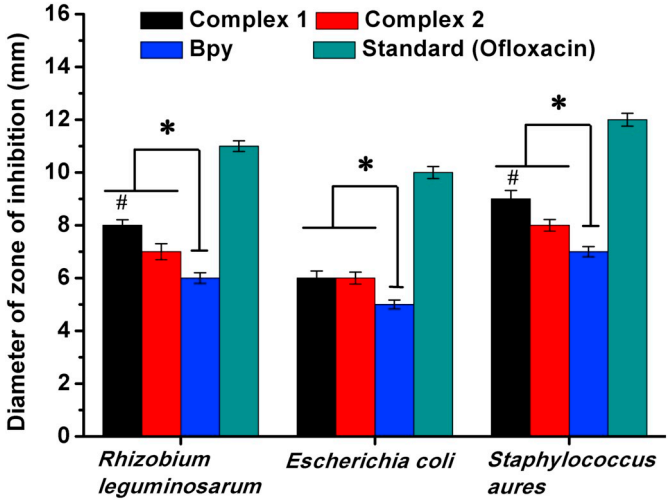

Fig. 5. Zone of inhibition (mm) of the complexes and the ligand at minimum inhibitory concentrations. Data are mean ± S.D., $n = 3$, $^*p \le 0.05$ as compared to bpy and $\#p \le 0.05$ as compared to complex **2**. (For interpretation of the references to color in this figure, the reader is referred to the web version of this article.)

Table 1
Antibacterial activity of complexes **1**, **2** and bpy at minimum inhibitory concentrations.

Compounds	Diameter of zone of inhibition (in mm)		
	Rhizobium Leguminosarum (MTCC99)	*Escherichia coli* (MTCC448)	*Staphylococcus aureus* (MTCC3160)
bpy	6 ± 0.17	5 ± 0.20	7 ± 0.19
Complex **1**	8 ± 0.21	6 ± 0.18	9 ± 0.24
Complex **2**	7 ± 0.18	6 ± 0.22	8 ± 0.18
Ofloxacin	11 ± 0.25	10 ± 0.24	12 ± 0.32

Table 2
Minimum inhibitory concentration (MIC) ($\mu g \cdot mL^{-1}$) and % activity index (in parenthesis) at MIC for **1**, **2** and bpy.

Compounds	*Rhizobium leguminosarum* (MTCC99)	*Escherichia coli* (MTCC448)	*Staphylococcus aureus* (MTCC3160)
bpy	350 (54.5%)	450 (50%)	350 (58.3%)
Complex **1**	125 (72.7%)	250 (60%)	125 (75%)
Complex **2**	250 (63.6%)	350 (60%)	250 (66.6%)
Ofloxacin	0.125 (23%)	0.332 (16%)	0.21 (25%)

Rhizoctonia Solani (MTCC4633) but showed no significant activity under the assay conditions. The complex **1** showed better antibacterial activity compared to complex **2** (see Fig. S9).

3.5. MTT based cell viability assay and IC_{50} measurement

The cytotoxic effects of **1** and **2** on cancer (DL) and normal (PBMC) cells were evaluated using MTT assay. MTT assay is important step in the search for new drugs and it is considered to be one of the most important preliminary screening method for natural products and synthetic compounds for studying cell proliferation and anticancer activity [53–54]. The analyses of cell viability results obtained for both compounds on DL cell line treated for 24 h showed significant concentration dependent decrease ($P \leq 0.05$) in cell viability. 35–50% cell cytotoxicity was obtained for both compounds at the dose range of 1-10 μM within 24 h. At the same time, negligible *cytotoxic* effect (~10%) was observed against *normal* PBMC cells as compared to cancer cell (DL). The results of the IC_{50} data (μM) for the antitumor activities are shown in Table 3, along with the data obtained for positive reference drug, *cis*-platin. The analyses of mean IC_{50} using concentration-response curves obtained for *cis*-platin, **1** and **2** were 0.45, 15.21 and 17.12 respectively. In another study, bipyridine complexes have been demonstrated to be most cytotoxic in prostate, breast, ovarian and Hodgkin lymphoma cells with IC_{50} values lower than the reference drug cisplatin [55] (see Fig. 6).

3.6. Apoptosis study using fluorescence microscope

Apoptosis is a physiological process of cell death that occurs naturally when cell age or it may be induced externally by chemical agents. It is characterized by morphological features and mainly associated with severe DNA damage, the frequency and time of appearance of which depend on the cell line and the apoptosis-inducing signal [56]. In order to investigate the action of compounds on morphological changes in DL cells, acridine orange (AO)/ethidium bromide (EB) dual staining method were used under fluorescence microscopy. Since AO is a crucial dye that can stain nuclear DNA of viable cells with intact cell membrane and uniformly stained green, whereas EB can only stain cells that had lost their membrane integrity [57] and appears red or orange. The results of apoptotic study in control group showed mostly viable DL cells identified by bright uniform green nuclei with organized cell membrane structures (see Fig. 7). Compounds **1** and **2** treated cells showed concentration-dependent increase in apoptotic features in DL cells. Lower

Table 3
IC_{50} values of *cis*-platin, compounds **1** and **2** on DL and PBMC cells.

Sl nos.	Reference drug/compounds	IC_{50} (μM)	
		DL cells (Cancer cells)	PBMC (Normal cells)
1	*cis*-platin	0.45	06.31
2	Compound **1**	15.21	59.13
3	Compound **2**	17.12	63.23

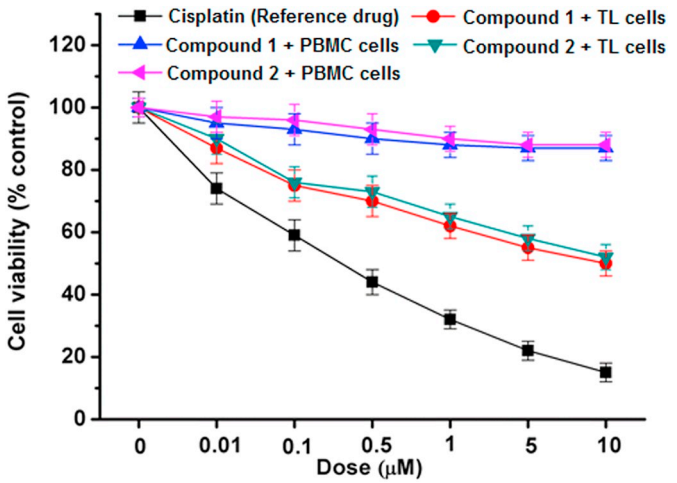

Fig. 6. Cell viability study on DL and PBMC cells after treatment with compound **1** and **2** along with reference drug, *cis*-platin at different dosage (0.01–10 μM) for 24 h. Data are mean ± S.D., $n = 3$. (For interpretation of the references to color in this figure, the reader is referred to the web version of this article.)

concentration such as 0.5 μM showed mostly early apoptotic cells with nuclear marginalization and chromatin condensation. Whereas higher concentration, 1 and 5 μM showed late apoptotic features which includes fragmented chromatin, cytoplasmic vacuoles and apoptotic bodies (under 100×). DNA has been identified as a primary target for developing anticancer drug and remains one of the most promising biological targets for the development of chemotherapeutic agents. The results suggested that both compounds were able to induce apoptosis in DL cells. Moreover, it can be seen that cisplatin induced more apoptotic cell death against DL cells than that of both compounds. The obtained higher cytotoxicity (MTT assay) and apoptosis induced by *cis*-platin may be due to the ability of *cis*-platin to crosslink with the purine bases of target DNA; interfering with cellular DNA repair mechanisms, causing bulky DNA due to intercalation followed by severe DNA damage and subsequently inducing apoptosis in cancer cells [58]. However, because of drug resistance and numerous undesirable side effects have also been reported with *cis*-platin treatment. Furthermore, combination therapies of *cis*-platin with other drugs have been successfully used to overcome drug-resistance and toxicity in the host [59]. It has also been reported that pyridine derivatives induce cancer cell apoptosis by triggering DNA damage-mediated p53 phosphorylation in A375 cells [60]. Ruthenium pyridyl complexes have also been demonstrated potent antiproliferative activity, and induce mitochondria-mediated and caspase-dependent apoptosis in human cancer cells through regulation of Bcl-2 family members and activation of caspases [61].

3.7. Molecular docking study

The potent cytotoxicity and apoptotic inducing features of synthesized compounds generated interest to perform molecular docking study to dissect possible mechanism associated with cytotoxicity and apoptosis due to interactions between cancer target proteins and compound under study. The receptors used in present study are closely involved at various stages of cell multiplication and hence responsible for the propagation of cancer [38–41]. Moreover, their inhibition by various chemotherapeutic agents is associated with the apoptotic induction and hence inhibition of cancer growth and invasion [62]. Docking was validated by redocking the original ligands present in active site of receptors as observed in crystallography pdb file (PDB ID 4XV2, 5LWE, 4FLH and 1XKK). The reference inhibitors for B-RAF kinase, CC chemokine receptor, EGFR kinase domain and PI3K- gamma receptors are Dabrafenib, vercirnon, quinazoline and AMG-511

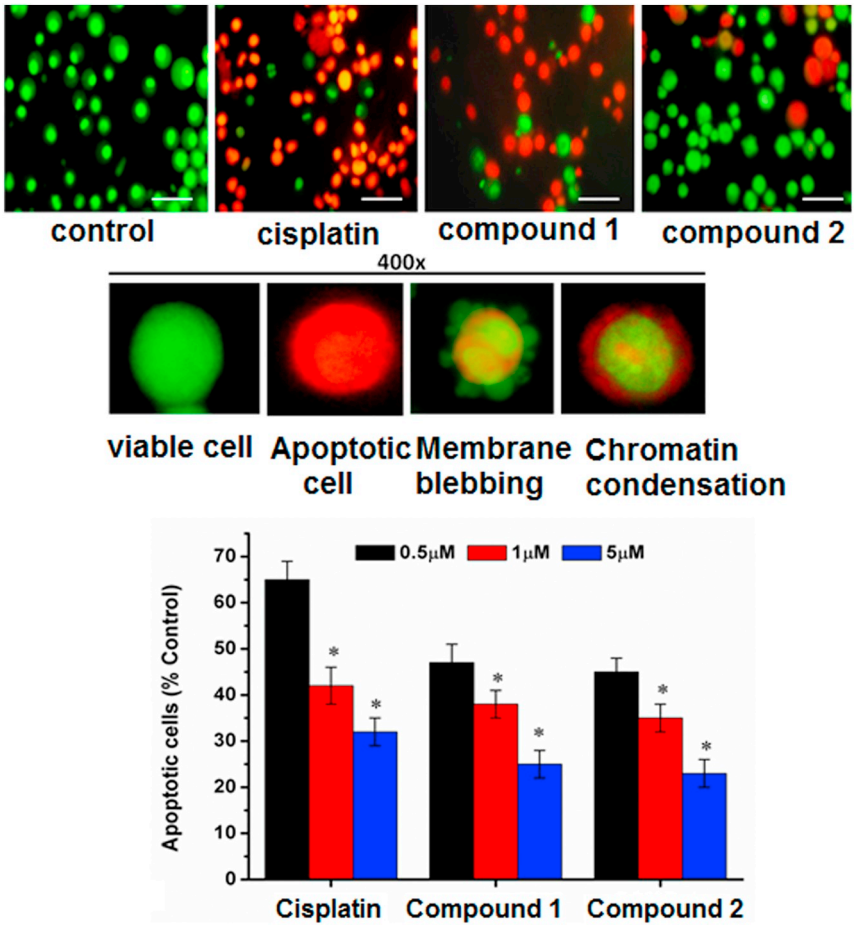

Fig. 7. Upper panel showed morphological features of apoptotic and viable cells with acridine orange and ethidium bromide (AO/EB) staining. Control DL cells showed mostly viable cells, *cis*-platin and complexes treated groups showing apoptotic features evident by red/orange nuclei with membrane damage and blebbing. Scale bar 10 μm. Lower panel showed percentage apoptotic cells after treatment with compounds and the reference drug, cisplatin at different dosage. Data are mean ± S.D., $n = 3$, ANOVA, $P \leq 0.05$.

respectively. Dabrafenib is an ATP-competitive inhibitor of BRAF with anti-tumor activity documented in melanoma and either untreated or locally treated brain metastases; interestingly dabrafenib mediated host toxicity is manageable [63]. Chemokines and their G-protein-coupled receptors play various role in immune defence, viral entry, tumor growth and metastasis and hence are important drug targets in a wide range of diseases. The selective CCR9 antagonist vercirnon progressed to phase 3 clinical trials that can be targeted for drug design, not only at CCR9, but potentially extending to other chemokine receptors [64]. Quinazoline derivatives have been reported for many different biological properties and recently, quinazolines have been shown to contain EGFR kinases inhibitory activities, useful to inhibit tumor growth [65]. PI3K signaling pathway is frequently activated in cancer and has been implicated in many aspects of tumor growth and survival. Inhibition of this pathway represents a potential therapeutic path for the treatment of cancer. AMG-511 is a potent and selective pan class I PI3K inhibitor [66]. The molecular docking studies revealed that the tested compounds were the most promising compounds, which is explained by lowest binding energy and hydrogen bonding with the exposed active site amino acids of target proteins of present study and that might be one of the reasons for cytotoxicity and inducing apoptosis in DL cells in in vitro studies (Figs. 8 and 9). The results in terms of docking scores are comparable to their respective reference inhibitors (Fig. 10) which were also docked with all the target proteins using similar parameters. The obtained hydrogen bond interactions between compound **1** and with active site amino acids of different target proteins are as follows: EGFR kinase domain: Cys797; PI3K- gamma receptors: Gln893, Ala805; B-RAF kinase: Cys532, Gly534; CC chemokine receptor: Arg144, Arg323, Thr83. Whereas, in case of compound **2** it was EGFR kinase domain: Cys797, Thr790; PI3K- gamma receptors: Lys807, Asp758, Lys809; B-RAF kinase: Cys797, asp855; CC chemokine receptor: Glu322, Thr256. Thus, based on the docking analysis, both complexes indicate anticancer activity which can be explained with their efficient interaction with cancer target proteins.

The *SAR analysis* of compound enables to identify specific *chemical* group(s) present in the molecular structure that is responsible for biological activities in the host [67]. The pharmacophore study also provides the key interaction features of a molecule responsible for enhancing or blocking biological activity. Ligand and structure-based pharmacophore models are comprised of features obtained from interactions between the exposed active site amino acids of receptor and the compounds. It is used to understand the key interaction features of a set of active molecules and about the interaction of the bioactive compound in the target-binding site [67,68]. The interactions derived from pharmacophore models for **1** and **2** revealed hydrophobic interactions with the aromatic rings. Positive ionizable interactions are observed with the nitrogen atoms of bipyridine (for both **1** and **2**) and pdc ligands (for **2**). The carboxylate O atoms in pdc and one of the bipyridine N atoms act as H-bond acceptors [68] (see Fig. 11).

4. Conclusion

Two new neutral coordination complexes of Mn(II) and Zn(II) involving 2,2′-bipyridine have been synthesized in water under ambient

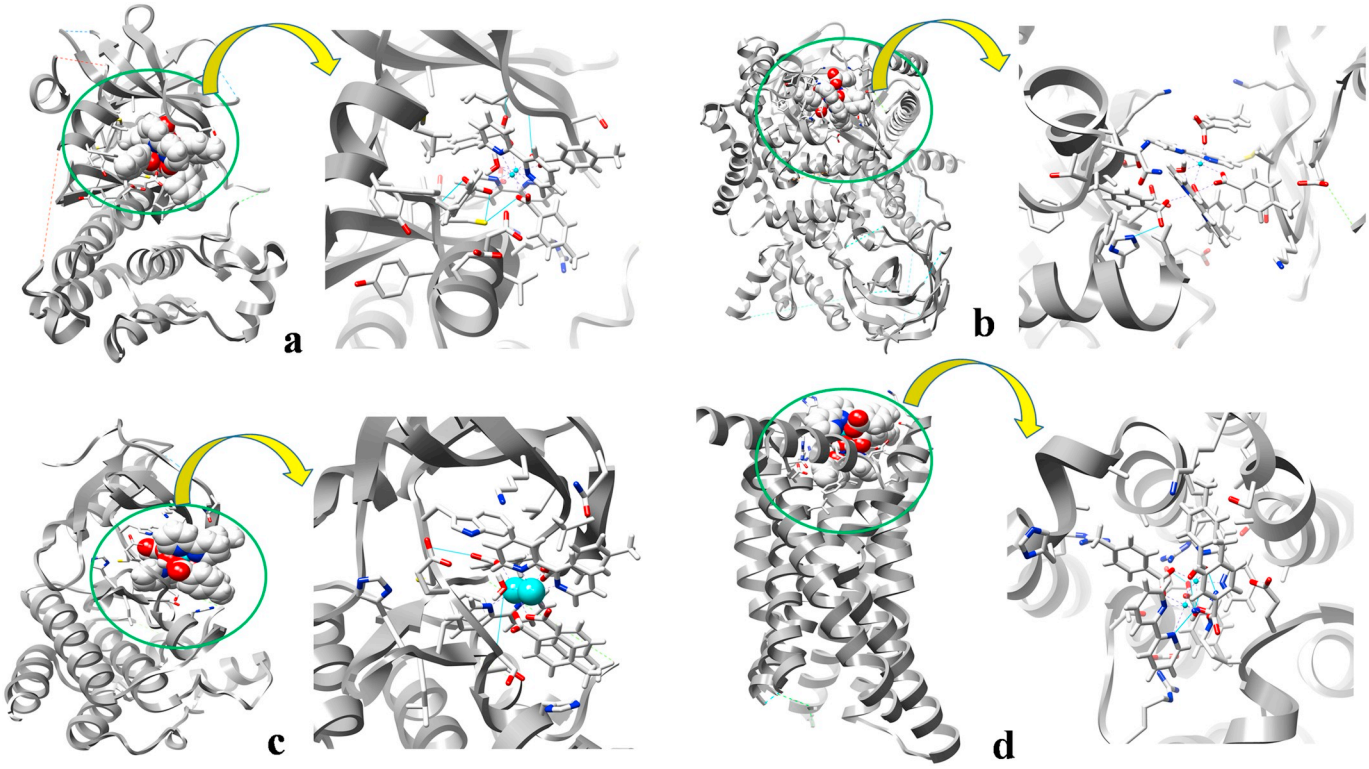

Fig. 8. Docking structure of compound **1** with EGFR kinase domain (a), PI3K- gamma receptors (b), B-RAF kinase (c) and (d) CC chemokine receptor. H-bond interactions are shown in blue lines in the inhibitors binding sites.

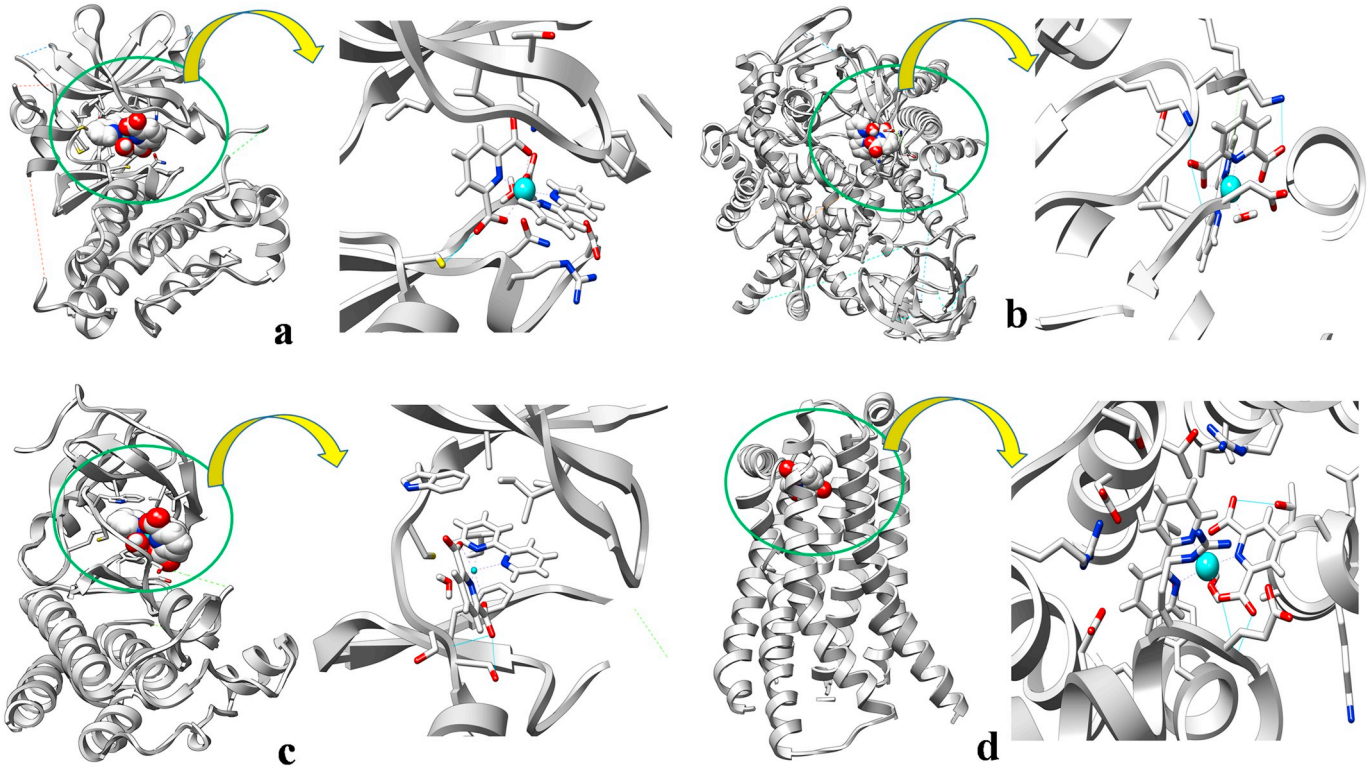

Fig. 9. Docking structure of compound **2** with EGFR kinase domain (a), PI3K- gamma receptors (b), B-RAF kinase (c) and (d) CC chemokine receptor. H-bond interactions are shown in blue lines in the inhibitors binding sites.

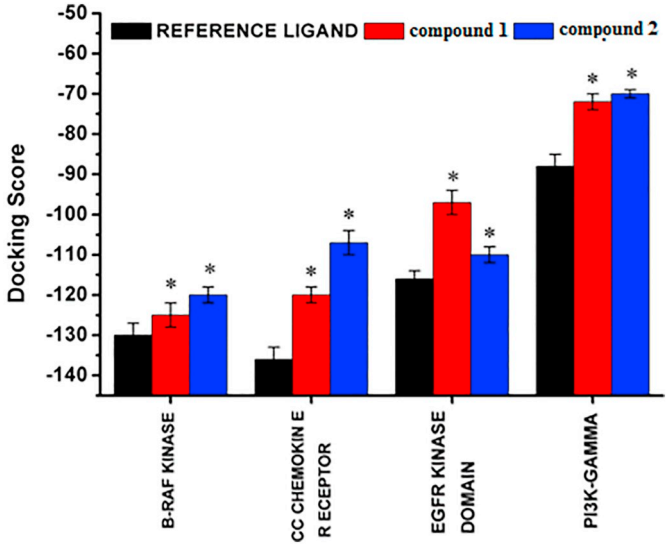

Fig. 10. Docking scores of compounds with B-RAF kinase, CC chemokine receptor, EGFR kinase domain and PI3K-gamma receptors. The reference inhibitors for B-RAF kinase, CC chemokine receptor, EGFR kinase domain and PI3K-gamma receptors are Dabrafenib, vercirnon, quinazoline and AMG-511 respectively. As per MVD docking score algorithm, lowest the score better is the interactions. Data are mean ± S.D., $n = 3$, ANOVA, $P \leq 0.05$. (For interpretation of the references to color in this figure, the reader is referred to the web version of this article.)

conditions and characterized by single crystal X-ray diffraction, electronic, vibrational spectroscopy, PXRD and TGA. The dimeric units of **1** self assembles into a 2D supramolecular architecture by π–π stacking, C—H···O hydrogen bonding and an unusual weak C—H···C contact. In the solid-state structure of **2**, the monomeric units arrange into a 2D architecture involving the interplay of strong π–π stacking and C—H···O hydrogen bonding interactions, which have been evaluated energetically and characterized using the NCI plot. Both the complexes showed antibacterial activity towards *Rhizobium Leguminosarum* (MTCC99), *Staphylococcus aureus* (MTCC-3160) and *E. coli* (MTCC448). The complex **1** showed better activity compared to **2**. Both compounds significantly ($P \leq 0.05$) inhibit cell viability by inducing apoptotic cell death in DL malignant cancer cells with negligible cytotoxic in normal cells. The molecular docking and SAR studies revealed that compounds were the most effective in inhibiting cancer target proteins and the result were in agreement with cytotoxicity assay. Therefore, these results strongly indicate the need for further preclinical evaluation to test the clinical potential of these new bipyridine complexes.

Acknowledgement

The authors acknowledge the financial support from University Grants Commission (UGC), New Delhi [Grant number: F. No. 42-377/2013]. The authors thank SAIF, Gauhati University, Guwahati for providing the single crystal X-ray diffraction data. Authors are thankful to the CSIR-NEIST, Jorhat for providing the PXRD data and Department of Chemistry, Gauhati University, Guwahati for providing the TGA data. We thank the MINECO/AEI of Spain (project CTQ2017-85821-R FEDER funds) for financial support. We thank the CTI (UIB) for computational

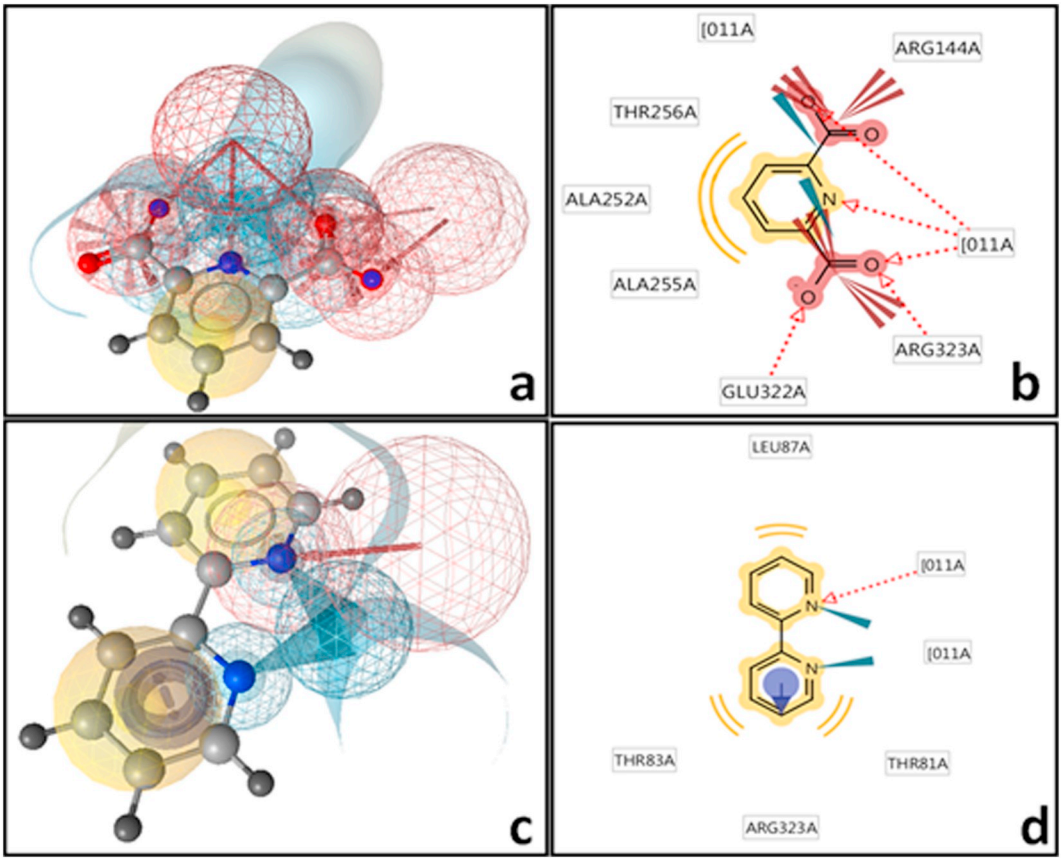

Fig. 11. Pharmacophore model showing the structural fragments responsible for biological activities of complexes **1** and **2**. Hydrophobic, positive ionizable, negative ionizable and acceptor interactions are depicted as yellow spheres, blue star, red star and red arrows, respectively (a and c). The 2D-depiction (b and d) illustrates a hydrophobic pocket with hydrophobic interactions with the binding site residues. Interactions derived and depicted using Ligandscout software.

facilities. A Franconetti thanks the MINECO/AEI of Spain for a "Juan de la Cierva" contract. Ligandscout software team is also acknowledged for providing license file for performing pharmacophore study.

Appendix A. Supplementary data

CCDC1872954 and1881306 contains the supplementary crystallographic data for **1** and **2** respectively. These data can be obtained free of charge at http://www.ccdc.cam.ac.uk or from the Cambridge Crystallographic Data Centre, 12 Union Road, Cambridge CB2 1EZ, UK; fax: (+44) 1223–336-033; or e-mail: deposit@ccdc.cam.ac.uk. Supplementary data to this article can be found online at https://doi.org/10.1016/j.jinorgbio.2019.110803.

References

[1] I. Romero, L. Dubois, M.N. Collomb, A. Deronzier, J.M. Latour, J. Pécaut, Inorg. Chem. 41 (2002) 1795–1806.
[2] B. Albela, M. Corbella, J. Ribas, I. Castro, J. Sletten, H. Stoeckli-Evans, Inorg. Chem. 37 (1998) 788–798.
[3] T. Glowiak, H. Kozlowski, L.S. Erre, G. Micera, Inorg. Chim. Acta 236 (1995) 149–154.
[4] S.B. Yu, S.J. Lippard, I. Shweky, A. Bino, Inorg. Chem. 31 (1992) 3502–3504.
[5] M. Atta, P. Nordlund, A. Aberg, H. Eklund, M. Fontecave, J. Biol. Chem. 267 (1992) 891–894.
[6] D. Deng, P. Liu, W. Fu, L. Li, F. Yang, B. Ji, Inorg. Chim. Acta 363 (2010) 891–898.
[7] J.C. MacDonald, P.C. Dorrestein, M.M. Pilley, M.M. Foote, J.L. Lundburg, R.W. Henning, A.J. Schultz, J.L. Manson, J. Am. Chem. Soc. 122 (2000) 11692–11702.
[8] C.G. Saysell, C.D. Borman, A.J. Baron, M.J. McPherson, A.G. Sykes, Inorg. Chem. 36 (1997) 4520–4525.
[9] L. Yang, D.C. Crans, S.M. Miller, A. Cour, O.P. Anderson, P.M. Kaszynski, M.E. Godzala, L.T.D. Austin, G.R. Willsky, Inorg. Chem. 41 (2002) 4859–4871.
[10] G. Scapin, S.G. Reddy, R. Zheng, J.S. Blanchard, Biochemistry 36 (1997) 15081–15088.
[11] B.L. Martin, Arch. Biochem. Biophys. 345 (1997) 332–338.
[12] B. Zhao, X.Y. Chen, Z. Chen, W. Shi, P. Cheng, S.P. Yan, Chem. Comm. (2009) 3113–3115.
[13] B. Das, J.B. Baruah, Inorg. Chim. Acta 363 (2010) 1479–1487.
[14] B. Das, J.B. Baruah, Polyhedron 30 (2011) 22–26.
[15] B. Das, J.B. Baruah, Polyhedron 31 (2012) 361–367.
[16] E.E. Sileo, M.A. Blesa, G. Rigotti, B.E. Rivero, E.E. Castellano, Polyhedron 15 (1996) 4531–4540.
[17] N. Okabe, N. Oya, Acta Cryst. C 56 (2000) 305.
[18] M. Yaman, G. Kaya, H. Yekeler, World J. Gastroenterol. 13 (2007) 612–618.
[19] S. Dasari, P.B. Tchounwou, Eur. J. Pharmacol. 740 (2014) 364–378.
[20] P. Zhao, M.C. Liu, M. Zheng, S. Jin, D. Tang, J. Chen, Y. Ma, J. Lin, X. Wang, H. Liu, Dyes Pigments 128 (2016) 41–48.
[21] J.N. Liu, W.B. Bu, L.M. Pan, J.L. Shi, Angew. Chem. 125 (2013) 4471–4475.
[22] B.J.M. Leite Ferreira, P. Brandão, M. Meireles, F. Martel, A. Correia-Branco, D.M. Fernandes, T.M. Santos, V. Félix, J. Inorg. Biochem. 161 (2016) 9–17.
[23] A.G. Majouga, M.I. Zvereva, M.P. Rubtsova, D.A. Skvortsov, A.V. Mironov, D.M. Azhibek, O.O. Krasnovskaya, V.M. Gerasimov, A.V. Udina, N.I. Vorozhtsov, E.K. Beloglazkina, L. Agron, L.V. Mikhina, A.V. Tretyakova, N.V. Zyk, N.S. Zefirov, A.V. Kabanov, O.A. Dontsova, J. Med. Chem. 57 (2014) 6252–6258.
[24] K. Ghosh, P. Kumar, N. Tyagi, U.P. Singh, V. Aggarwal, M.C. Baratto, Eur. J. Med. Chem. 45 (2010) 3770–3779.
[25] G.M. Sheldrick, Acta Crystallogr. A 64 (2008) 112.
[26] L.J. Farrugia, J. Appl. Crystallogr. 32 (1999) 837.
[27] K. Brandenburg, Diamond 3.1f, Crystal Impact GbR, Bonn, Germany, (2008).
[28] M.J. Frisch, G.W. Trucks, H.B. Schlegel, G.E. Scuseria, M.A. Robb, J.R. Cheeseman, G. Scalmani, V. Barone, G.A. Petersson, H. Nakatsuji, X. Li, M. Caricato, A. Marenich, J. Bloino, B.G. Janesko, R. Gomperts, B. Mennucci, H.P. Hratchian, J.V. Ortiz, A.F. Izmaylov, J.L. Sonnenberg, D. Williams-Young, F. Ding, F. Lipparini, F. Egidi, J. Goings, B. Peng, A. Petrone, T. Henderson, D. Ranasinghe, V.G. Zakrzewski, J. Gao, N. Rega, G. Zheng, W. Liang, M. Hada, M. Ehara, K. Toyota, R. Fukuda, J. Hasegawa, M. Ishida, T. Nakajima, Y. Honda, O. Kitao, H. Nakai, T. Vreven, K. Throssell, J.A. Montgomery, Jr., J.E. Peralta, F. Ogliaro, M. Bearpark, J.J. Heyd, E. Brothers, K.N. Kudin, V.N. Staroverov, T. Keith, R. Kobayashi, J. Normand, K. Raghavachari, A. Rendell, J.C. Burant, S.S. Iyengar, J. Tomasi, M. Cossi, J.M. Millam, M. Klene, C. Adamo, R. Cammi, J.W. Ochterski, R.L. Martin, K. Morokuma, O. Farkas, J.B. Foresman, D.J. Fox, Gaussian 09, Revision C.02, Gaussian, Inc., Wallingford CT, 2016.
[29] S. Grimme, J. Antony, S. Ehrlich, H. Krieg, J. Chem. Phys. 132 (2010) 154104.
[30] (a) J. Adhikary, P. Chakraborty, S. Das, T. Chattopadhyay, A. Bauza, S.K. Chattopadhyay, B. Ghosh, F.A. Mautner, A. Frontera, D. Das, Inorg. Chem. 52 (2013) 13442–13452;
(b) M. Servati Gargari, V. Stilinović, A. Bauzá, A. Frontera, P. McArdle, D. Van Derveer, S.W. Ng, G. Mahmoudi, Chem Eur. J. (49) (2015) 17951–17958;
(c) M. Mirzaei, H. Eshtiagh-Hosseini, Z. Bolouri, Z. Rahmati, A. Esmaeilzadeh, A. Hassanpoor, A. Bauza, P. Ballester, M. Barceló-Oliver, J.T. Mague, B. Notash, A. Frontera, Cryst. Growth Des. 15 (2015) 1351–1361.
[31] J. Contreras-García, E.R. Johnson, S. Keinan, R. Chaudret, J.-P. Piquemal, D.N. Beratan, W. Yang, J. Chem. Theory Comput. 7 (2011) 625–632.
[32] E.R. Johnson, S. Keinan, P. Mori-Sanchez, J. Contreras-Garcia, A.J. Cohen, W. Yang, J. Am. Chem. Soc. 132 (2010) 6498–6506.
[33] T. Mosmann, J. Immunol. Methods 16 (1983) 55–63.
[34] A.K. Verma, S.B. Prasad, Anti Cancer Agents Med. Chem. 13 (2013) 1096–1114.
[35] Z.K. Ali, Haitham, M. Kadhim, H.B. Sahib, Int. J. Pharm. Sci. Rev. Res. 41 (2016) 363–366.
[36] M.K. Squier, J.J. Cohen, Mol. Biotechnol. 19 (2001) 305–312.
[37] S.B. Prasad, A.K. Verma, Microsc. Microanal. 19 (2013) 1377–1394.
[38] R. Thomsen, M.H. Christensen, J. Med. Chem. 49 (2006) 3315–3321.
[39] X. Ma, H. Yu, Yale J. Biol. Med 79 (2006) 85–94.
[40] P. Kumar, B. Narasimhan, K. Ramasamy, V. Mani, R.K. Mishra, A.B.A. Majeed, Curr. Top. Med. Chem. 15 (2015) 1050–1064.
[41] H. Bahron, S.S. Khaidir, A.M. Tajuddin, K. Ramasamy, B.M. Yamin, Polyhedron 161 (2019) 84–92.
[42] T. Mosmann, J. Immunol. Methods 65 (1983) 55–63.
[43] A. Swargiary, A.K. Verma, K. Sarma, Med. Chem. Res. 22 (2012) 2870–2878.
[44] M.A. Al-Sha'er, Q.A. Al-Balas, M.A. Hassan, G.A. Al Jabal, A.M. Almaaytah, Comput. Biol. Chem. 80 (2019) 102–110.
[45] G. Wolber, T. Langer, J. Chem. Inf. Model. 45 (2005) 160–169.
[46] (a) D. Dutta, S. Chetry, A. Gogoi, B. Choudhury, A.K. Guha, M.K. Bhattacharyya, Polyhedron 151 (2018) 381–393;
(b) M.K. Bhattacharyya, U. Saha, D. Dutta, A. Das, A.K. Verma, A. Frontera, RSC Adv. 9 (2019) 16339–16356.
[47] D. Deng, P. Liu, W. Fu, L. Li, F. Yang, B. Ji, Inorg. Chim. Acta 363 (2010) 891–898.
[48] A. Schaate, S. Klingelhöfer, P. Behrens, M. Wiebcke, Cryst. Growth Des. 8 (2008) 3200–3205.
[49] E.K. Efthimiadou, G. Psomas, Y. Sanakis, N. Katsaros, A. Karaliota, J. Inorg. Biochem. 101 (2007) 525–535.
[50] (a) A.D. Russell, in: S.S. Block (Ed.), Disinfection, Sterilization and Preservation, fourth ed., Lea and Febinger, Philadelphia, (1991) 27-59; (b) H.W. Rossmore, in: S.S. Block (Ed.), Disinfection, Sterilization and Preservation, fourth ed., Lea and Febinger, Philadelphia, 1991, pp. 290–321.
[51] G.Y.S.K. Swamy, P. Sivanarayanan, B. Sridhar, L.R. Joshi, J. Coord. Chem. 69 (2016) 1602–1617.
[52] M.S. Aljahdali, Eur. J. Chem. 4 (2013) 434–443.
[53] R.R. Teixeira, L.C. Barbosa, C.R.A. Maltha, M.E. Rocha, D.P. Bezerra, L.V. Costa-Lotuf, C. Pessoa, M.O. Moraes, Molecules 12 (2007) 1101–1116.
[54] A. Jamalian, R. Miri, O. Firuzi, M. Amini, A. Moosavi-Movahedi, A. Shafieea, J. Iran. Chem. Soc. 8 (2011) 983–991.
[55] M. Altaf, M. Monim-ul-Mehboob, A.N. Kawde, G. Corona, R. Larcher, M. Ogasawara, N. Casagrande, M. Celegato, C. Borghese, Z.H. Siddik, Oncotarget 8 (2017) 490–505.
[56] J. Wu, W. Yi, L. Jin, D. Hu, B. Song, Cell Div 7 (2012) 20.
[57] X. Xu, X. Gao, L. Jin, P.S. Bhadury, K. Yuan, D. Hu, B. Song, S. Yang, Cell Div 6 (2011) 14.
[58] D. Shaloam, P.B. Tchounwou, Eur. J. Pharmacol. 740 (2014) 364–378.
[59] D.S. Goodsell, Oncologist 11 (3) (2006) 316–317.
[60] L. Li, W. Cao, W. Zheng, C. Fan, T. Chen, Dalton Trans. 41 (2012) 12766–12772.
[61] T. Chen, Y. Liu, W.J. Zheng, J. Liu, Y.S. Wong, Inorg. Chem. 49 (2010) 6366–6368.
[62] S. Lee, E. Heinrich, J. Lu, W. Lee, A. Choi, C. Luu, V. Chung, M. Fakih, J. Kim, Pancreas 45 (2016) 286–292.
[63] J.J. Luke, F.S. Hodi, Oncologist 18 (2013) 717–725.
[64] C. Oswald, M. Rappas, J. Kean, A.S. Dore, J.C. Errey, K. Bennett, F. Deflorian, J.A. Christopher, A. Jazayeri, J.S. Mason, M. Congreve, Nature 540 (2016) 4735–4779.
[65] R.S. Ismail, N.S. Ismail, S. Abuserii, D.A.A. El Ella, Fut J Pharm Sci 2 (2016) 9–19.
[66] M.H. Norman, K.L. Andrews, Y.Y. Bo, S.K. Booker, S. Caenepeel, V.J. Cee, N.D. Dangelo, D.J. Freeman, B.J. Herberich, F.T. Hong, C.L. Jackson, J. Med. Chem. 55 (2012) 7796–7816.
[67] M.A. Peterson, M. Oliveira, M.A. Christiansen, C.E. Cutler, Bioorg. Med. Chem. Lett. 19 (2009) 6775–6779.
[68] M. Muchtaridi, H. Syahidah, A. Subarnas, M. Yusuf, S. Bryant, T. Langer, Pharmaceuticals 10 (2017) 81.